

**Performance Limits of Micro-Actuation with Vanadium Dioxide as a Solid Engine**

Kevin Wang, Chun Cheng, Edy Cardona, Jingyang Guan, Kai Liu, Junqiao Wu

**1. Wind actuation (Movie 1).**

Video of the bimorph actuation via wind cooling is shown in Movie 1. Here, the substrate is heated to 69 °C, and 500 sccm of wind is directed in a direction opposite to the bimorph bending (inwards, increasing curvature). The observed bending amplitude is very large ( $A/L \sim 0.8$ ), but the duty cycle is moderate to low (< 50%).

At higher substrate temperatures, the VO<sub>2</sub>/Cr bimorph becomes increasingly difficult to cool across the metal-insulator phase transition (MIT), resulting in smaller amplitude in oscillation. Increasing wind speed does not increase the amplitude greatly, but it noticeably increases the oscillation duty cycle. That is, for any given period of observation time, stronger wind causes more instances of bimorph actuation and lowers the time percentage that the bimorph stays stationary. The duty cycle is characterized as low, medium, or high depending on the percentage of times the bimorph is oscillating between the straight and bent states, as observed in the videos collected. The results of these trials at substrate temperatures of 68 and 75 °C for 3 different wind speeds are listed in Tab. S1.

Substrate Temperature	Wind Flow (sccm)	Nominal amplitude ( $\mu\text{m}$ )	Oscillation Duty Cycle
68 °C	200	230	Low
	500	238	Medium
	2000	235	Medium
75 °C	200	206	Low
	500	181	Medium
	2000	201	High

Tab. S1. Bending amplitude and qualitative switching duty of a cantilevered bimorph under various wind flow rates and two substrate temperatures. The bimorph is VO<sub>2</sub>(1  $\mu\text{m}$ )/Cr(0.3  $\mu\text{m}$ ) with length  $L = 217 \mu\text{m}$  and width  $a = 1 \mu\text{m}$ . Amplitude error is  $\pm 5 \mu\text{m}$ .

**2. Laser actuation in water (Movie 2).**

Movie 2 shows the bending of a bimorph soaked in de-ionized water and activated with a laser beam turned repeatedly on and off. By analyzing individual video frames, it is found that the bimorph completes bending within the time lapse between two consecutive frames. The

video frame rate is 60/sec, giving an upper limit of the response time of ~17 msec and lower frequency limit of 60Hz. The actual speed should be much faster.

The amplitude response of the device shown is much lower than that shown in the main text, Fig. 4c, due to the illumination point far from the base, exciting a reduced region to phase transition. Additionally, the Cr has started delaminating, visibly peeling from the base of the bimorph and causing discontinuities along the bimorph length. The loss of bonding between the two layers dramatically reduces the net strain difference in the bimorph, reducing the amplitude change. Physical degradation like this can be prevented by a more careful Cr deposition, followed by a post-deposition anneal.

### 3. Nucleation of the M2 phase at intermediate temperatures.

From the strain-temperature phase diagram (Fig.1c), we expect the M2 phase to be stable at intermediate temperatures under tensile strain. We attribute the nucleation of M2 in the bimorphs to be at the free side of the curved VO<sub>2</sub> nanobeam, which is under tensile strain. Cr diffusion into VO<sub>2</sub> at the VO<sub>2</sub>/Cr interface also tends to stabilize the M2 structure,<sup>1</sup> but this is unlikely the leading effect here, since the Cr deposition and rapid anneal at 250 °C is not expected to diffuse much Cr into the VO<sub>2</sub> nanobeam.

### 4. Pulsed laser actuation (Movie 3, Movie 4).

The bimorph actuation can be analyzed by decomposing the total oscillation amplitude into inward bending amplitude  $A^{M2}$  (from the unperturbed position towards the max M2 position) and outward bending amplitude  $A^R$  (from the unperturbed position towards the max R position), so that the total amplitude  $A(f) = A^{M2}(f) + A^R(f)$ . By plotting the two oscillation amplitudes separately, we see that the rise in  $A(f)$  at intermediate  $f$  results from an increase in  $A^{M2}(f)$ , as shown in Fig. S1. This is explained by the limited cooling as the frequency rises. The peaking and eventual decrease of  $A^{M2}(f)$  at higher  $f$  also occur due to the cooling limitations – the VO<sub>2</sub> is unable to cool to a sufficiently low temperature, not even able to reach the M2 phase, and therefore stays in the heated R phase during the entire time of laser pulsing. The results with varying frequency at 3 positions along this bimorph are shown in Fig. S1. A sustained outward bending behavior can be seen for  $x/L = 0.3$ , producing considerable bending up to high frequencies. The high performance may represent an optimal excitation position on this bimorph, maximizing both “sub” and “air” modes of heat transfer and increasing the operating speed of the device.

By comparing the  $A(f)$  dependence between bimorphs of various cross section areas, we can better understand the “air” term of heat dissipation. Figure S2 plots  $A(f)$  for 3 bimorphs and reveals an improving high-frequency performance as the VO<sub>2</sub> thickness decreases. The peak displacements occur at frequencies of ~ 1, 2, and 3 kHz for bimorphs with VO<sub>2</sub> nanobeam thickness of 1, 0.9 and 0.7 μm respectively. This agrees with the predicted behavior, since the thinner bimorph has a greater surface to volume ratio, which increases the efficacy of the heat dissipation to air. Referring to the time constant  $\tau_{air}$  in the main text, the characteristic frequency

is inversely proportional to the “effective bimorph diameter”,  $ab/(a + b)$ . This qualitatively agrees with our observation of higher  $f_{-3\text{dB}}$  at smaller bimorph thickness.

Due to the fixed laser intensity, the outward oscillation towards R phase ( $A^R(f)$ ), shown in Fig. S1, cannot increase with  $f$ . The eventual decline in  $A^R(f)$  may be attributed to a negative feedback effect inherent in the sideways deflection of the experiment. The laser is directed at a point to heat the bimorph in its straight state, and the bimorph absorbs most of the incident laser energy under continuous and low frequency laser operation. At higher frequency operation, the nanobeam spends more time away from the initial state, settling instead in the inward or M2 bending region when the laser is chopped to be off. Consequently, when the laser pulse switches back on, less of the bimorph is in the pathway and less incident energy is absorbed, which reduces the total displacement and heating back towards the R position. It is possible that an alternate experimental setup, with nanobeam oscillation in the plane of the laser beam, could yield high tip displacement performance at even higher frequencies. In this hypothetical setup, the inward (M2) bending is expected first to decline to zero with further inability to cool, followed by the decrease of R-phase bending at high frequencies. Here, the displacement would saturate into the maximum R position. In this regime, the bimorph is unable to cool even to M2 temperatures, and retains the laser-induced R-phase, producing the same displacement that occurs at a continuous laser irradiation. Nonetheless, even given these limitations, the nanobeam bimorphs respond with outward R phase displacements at very high frequencies. From Fig. 4(c), the 3dB-attenuation frequency is 2.5kHz, solely considering outward bending.

Videos of actuation by laser are shown for a 217  $\mu\text{m}$  long bimorph with thickness  $\text{VO}_2(1 \mu\text{m})/\text{Cr}(0.3 \mu\text{m})$ , and width 1  $\mu\text{m}$ . A low-frequency (10 Hz) chopped laser results in M1-R switching, while high-frequency (2kHz) results in primarily M1-M2, as shown in Movies 3 and 4, respectively.

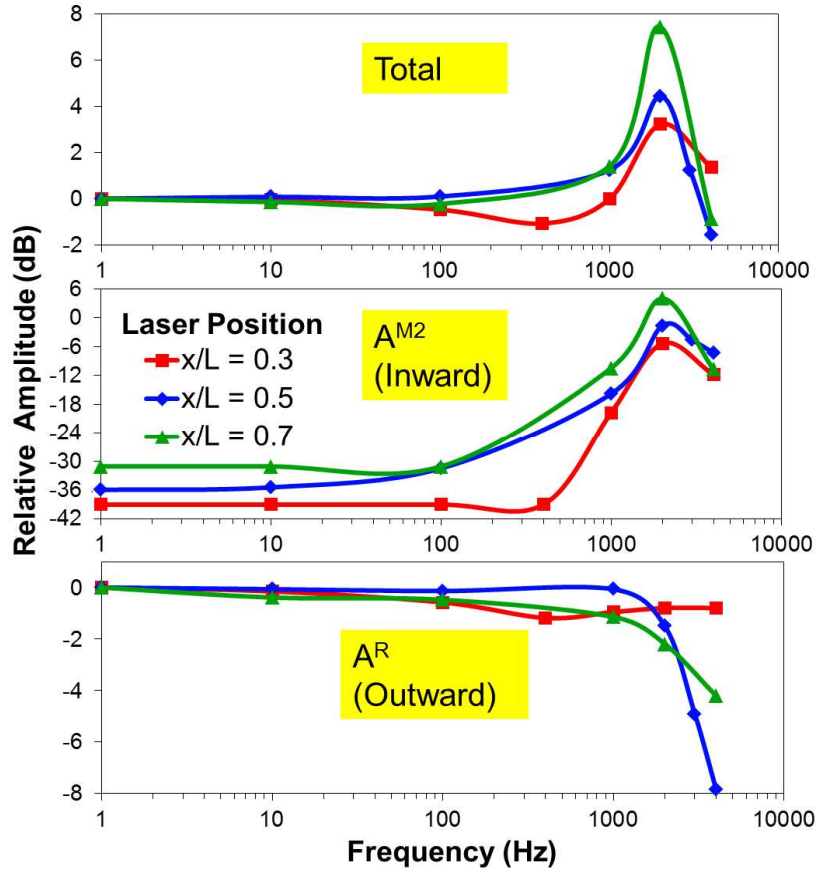


Fig. S1. Decomposition of the total amplitude into M2 amplitude and R amplitude shows the different frequency behavior of the actuation driven by the M1-M2 and M1-R transition. Colored lines are provided as a visual aid. Three laser positions are shown.

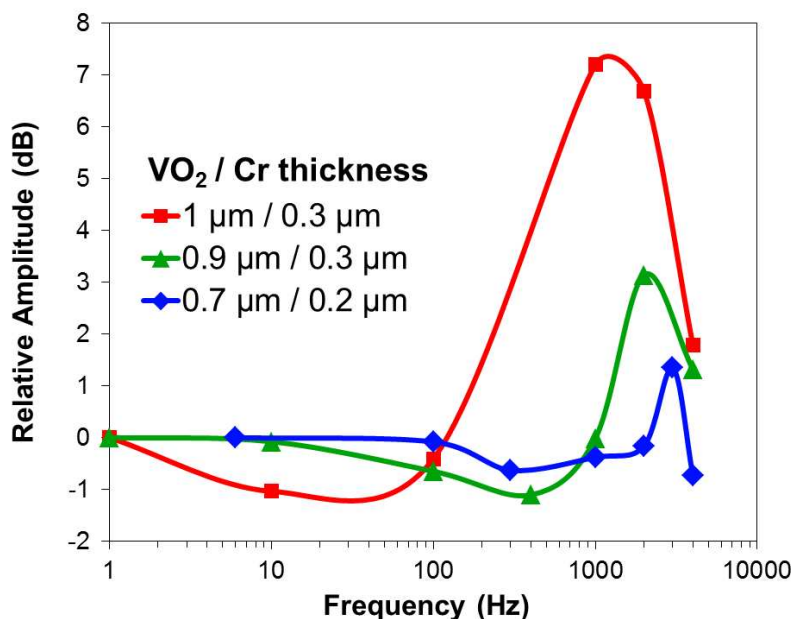


Fig.S2. Frequency response of actuation of 3 cantilevers with different VO<sub>2</sub> thickness. Bimorphs have similar width. Lengths are 100, 115, and 217 μm, respectively. The laser power is fixed for the experiments, and the focal position along the bimorph is fixed at  $x/L \sim 0.4$  for all three curves.

### 5. Self-oscillation (Movie 5).

An intriguing observation is a natural self-oscillation effect: even at un-chopped, continuous laser incidence, a heated bimorph will absorb energy, deflect, cool and then return back towards the laser in a steady, fast cycle. This process can be further studied to shed insight on the heat transfer dynamics. Movie 5 shows this effect for a bimorph of thickness VO<sub>2</sub>(1 μm)/Cr(0.3 μm), length 100 μm, and width 1 μm, for an incident laser power of 0.6 mW. By positioning the laser at the nanowire edge opposite to the inward (M2) bending direction, we can verify the negative feedback mechanism observe a natural oscillation in bending. As we move the laser away from its initial position towards the R position, we can induce an increased self-oscillation amplitude. The bimorph increases its R phase deflection and M2 deflection, as it accumulates more heat by coinciding more along the laser beam path.

### 6. Hybrid bimorph film (Movie 6).

A macroscopic PDMS film with dense and aligned VO<sub>2</sub>/Cr bimorphs embedded produced very large actuation amplitudes. Movie 6 shows the response as temperature is varied from 25 °C to 120 °C for a film measuring length 2mm, width 1mm, and thickness 20 μm. The maximum response (amplitude change) occurs in the 70 – 90 °C range, as this temperature at the global heat source results in local temperatures in the film around the phase transition of 68 °C. The bending amplitude ratio was measured to be  $A/L = 0.9$ , close to but not as high as that in global heating ( $A/L = 1.2$ ) of single bimorphs. There is a small inward bending of the bimorph film as it is heated from 25 °C to 37 °C, indicative of the M2 phase transition.

## 7. Energy efficiency calculation.

For a linear micro solid engine ( $\mu$ SE) based on a  $\text{VO}_2$  beam oriented along  $c_R$  with length  $L$ , width  $a$ , and thickness  $b$ , the maximum energy efficiency can be calculated by

$$\eta_{linear} = \frac{E_{out}}{E_{in}} = \frac{L \cdot \varepsilon_0 \cdot \sigma_C \cdot a \cdot b}{Lab\rho c\Delta T + LabH}, \quad (\text{S1})$$

where  $\varepsilon_0$  is the transformation strain (analogous to volume change in the liquid-vapor transition,  $\approx 1\%$  for M1-R and  $2\%$  for M2-R),  $\sigma_C$  is the critical stress that would drive the phase transition at a given  $T$  (analogous to pressure in the liquid-vapor transition, and is the stress at the phase boundary in Fig.S3a),  $\rho$  represents density,  $c$  the specific heat, and  $H$  the latent heat.  $\Delta T = T_{MIT} - T_0 = 68^\circ\text{C} - 27^\circ\text{C}$ . The numerator in equation (S1) is the work output from a complete engine cycle as shown in Fig.S3a. The Clapeyron equation links  $\sigma_C$  to  $H$ ,

$$\frac{d\sigma_C}{dT} = \frac{H}{\varepsilon_0 \cdot T_{MIT}}. \quad (\text{S2})$$

Assuming a linear phase boundary,<sup>ii</sup> we have

$$\sigma_C = \frac{d\sigma_C}{dT} \cdot \Delta T = \frac{H \cdot \Delta T}{\varepsilon_0 \cdot T_{MIT}}. \quad (\text{S3})$$

Substituting into equation (S1), we obtain

$$\eta_{linear} = \frac{\Delta T}{T_{MIT}} \cdot \frac{1}{1 + \rho c\Delta T/H}. \quad (\text{S4})$$

This is equation (1) in the main text. We note that

$$\eta_{Carnot} = \frac{\Delta T}{T_{MIT}}. \quad (\text{S5})$$

As predicted by equation (S4), although the engine efficiency decreases as  $T_{low}$  moves toward  $T_{high} = T_{MIT}$ , its relative value would approach the Carnot efficiency if the engine is operated near the phase boundary ( $\Delta T \rightarrow 0$ ).

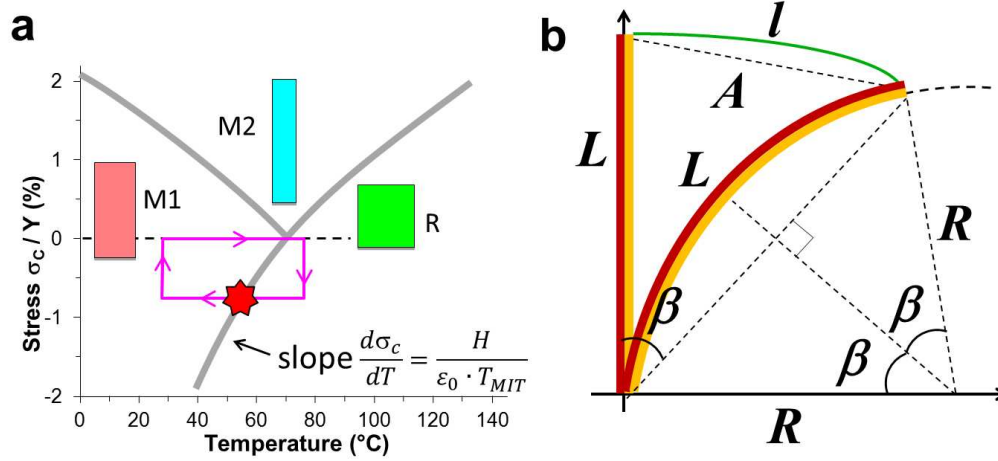


Fig. S3. **a.** The  $c_R$  stress – temperature phase diagram of VO<sub>2</sub>. The stress is normalized by the Young’s modulus. The Clapeyron equation relates the slope of the phase boundary to the latent heat of transition. The loop shows an engine cycle, where the red star is the point when work is done. **b.** Geometry of the bimorph system for energy efficiency calculation.

For the bimorph  $\mu$ SE coupling a VO<sub>2</sub> and a Cr layer, the efficiency calculation is more complicated. By treating the bimorph as a bilayer elastic beam with a spring constant, we can estimate the efficiency by dividing the mechanical work output at maximum displacement with the total heat absorbed (global heating). The spring constant is estimated from basic elastic beam theory,<sup>iii</sup>

$$k_{eff} = \frac{3a}{L^3} \cdot \frac{Y_1^2 b_1^4 + Y_2^2 b_2^4 + 2Y_1 b_1 Y_2 b_2 \cdot (2b_1^2 + 2b_2^2 + 3b_1 b_2)}{12(Y_1 b_1 + Y_2 b_2)}, \quad (S6)$$

where  $Y$  is the Young’s modulus ( $Y_{VO_2} \approx 140$  GPa and  $Y_{Cr} \approx 280$  GPa),  $L$  the length,  $a$  the width and  $b$  the thickness of the beam, and subscript “1” and “2” denote the VO<sub>2</sub> layer and the Cr layer, respectively. Defining the total curved path of the tip motion as  $l$  (Fig.S3b), the work output for a full bending cycle is then

$$E_{out} \approx 2 \cdot \frac{1}{2} k_{eff} l^2 \quad (S7)$$

Our system typically operates beyond the “small beam bending” limit, as the displacement is large,  $l/L \sim A/L \sim 1$ . However, we note that a simple scaling argument predicts the energy efficiency to be an intensive rather than extensive quantity, and be independent of the bimorph length  $L$ : a bimorph with length  $L$  outputs the same amount of work as two bimorphs each with length  $L/2$  connected in series. Therefore, for the efficiency calculation, we only need to calculate for bimorphs with maximum bending still within the linear deformation regime  $l/L \ll 1$ . This is the case for bimorphs with small  $L$ . This is because the bending curvature  $1/R$  is generally independent of the beam length  $L$  and is given solely by the thicknesses and Young’s moduli of the two layers,<sup>iv,v</sup>

$$\frac{1}{R} = \frac{6Y_1b_1Y_2b_2(b_1 + b_2)}{Y_1^2b_1^4 + Y_2^2b_2^4 + 2Y_1b_1Y_2b_2 \cdot (2b_1^2 + 2b_2^2 + 3b_1b_2)} \cdot \varepsilon_0, \quad (\text{S8})$$

where  $\varepsilon_0$  is the transformation strain. For the  $Y_1/Y_2$  ratio in our case, the largest  $1/R$  is given by  $b_2/b_1 \approx 0.4$ . Comparing bimorphs with the same  $b_1$  and  $b_2$  thicknesses and thus the same  $1/R$ , those with smaller  $L$  give not only smaller  $l$ , but also smaller  $l/L$ . In fact, it can be proved from the geometry in Fig.S3b that generally,

$$l/L = \int_0^{L/2R} \left| \frac{\sin \beta}{\beta} \right| d\beta. \quad (\text{S9})$$

At small deflection angles (*i.e.*, smaller  $L/2R$ ), we have  $l \approx L^2/2R$ . Thus we can utilize the bimorph spring constant  $k_{\text{eff}}$  in the low-deflection Hooke's law behavior given by equation (S7) to predict a work output linearly proportional to  $L$ . Since the energy input  $E_{\text{in}}$  is also proportional to  $L$ , the energy efficiency ( $\eta = E_{\text{out}}/E_{\text{in}}$ ) is therefore independent of  $L$ . As in the case of linear  $\mu\text{SE}$ , the energy input is given by

$$E_{\text{in}} \approx La(b_1\rho_1c_1 + b_2\rho_2c_2)\Delta T + Lab_1H, \quad (\text{S10})$$

where  $c_1$  is the specific heat of  $\text{VO}_2$  ( $\approx 690 \text{ J/kgK}$ ),<sup>vi</sup>  $c_2$  the specific heat of  $\text{Cr}$  ( $\approx 444 \text{ J/kgK}$ )<sup>vii</sup>, and  $H$  the latent heat of the MIT of  $\text{VO}_2$  ( $\approx 1000 \text{ Cal/mol} = 250 \text{ J/cm}^3$ ).<sup>viii</sup> A  $\text{VO}_2$  density  $\rho_1$  of  $4.66 \text{ g/cm}^3$  was used,<sup>ix</sup> along with a  $\text{Cr}$  density<sup>x</sup>  $\rho_2$  of  $7.19 \text{ g/cm}^3$ .

The calculated energy efficiencies are shown in Fig.1d in the main text, for bimorphs with  $L = 5 \mu\text{m}$  while varying the thickness. These efficiencies are compared to those of thermoelectrics operating between  $T_{\text{high}} = T_{\text{MIT}} = 68 \text{ }^\circ\text{C}$  and  $T_{\text{low}} = T_0 = 27 \text{ }^\circ\text{C}$ . Assuming the thermoelectric figure-of-merit to be  $ZT$ , the thermoelectric engine efficiency is given by,

$$\eta_{\text{TE}} = \frac{T_{\text{high}} - T_{\text{low}}}{T_{\text{high}}} \cdot \frac{\sqrt{1 + ZT} - 1}{\sqrt{1 + ZT} + T_{\text{low}}/T_{\text{high}}}. \quad (\text{S11})$$

We also would like to point out the difference between **intrinsic** energy loss and **extrinsic** energy loss in evaluation of efficiency in an energy conversion technology. Intrinsic loss is the fundamental, unavoidable loss that is attributed to the limit of the working material (such as the thermal conductivity and electrical conductivity of the material in thermoelectrics), while extrinsic loss is the avoidable loss attributed to realistic limit in a device design (such as the heat loss via air or packaging material, and energy loss due to contact resistance in thermoelectrics). Without the intrinsic loss, the efficiency would approach the Carnot efficiency. Without the extrinsic loss, the efficiency of thermoelectrics will be given by Eq.(S11).

In analogy, in our efficiency evaluation of  $\text{VO}_2 \mu\text{SE}$ , the intrinsic energy loss is indeed included, which is the heat needed to increase the  $\text{VO}_2$  temperature up to the MIT temperature (determined by the specific heat of  $\text{VO}_2$ , and completely lost during a cycle). Without this intrinsic loss term, the efficiency will be simply the Carnot efficiency. The extrinsic energy loss is the loss via air convection, or possible friction loss during actuation. Without the extrinsic loss, the efficiency is given Eq.(S4).

Therefore, to analyze the pure materials performance in the VO<sub>2</sub> engine, we believe it is indeed a fair and appropriate comparison, to compare the intrinsic efficiency predicted by Eq.(S4) in our case, to the intrinsic efficiency predicted by Eq.(S11) in the case of thermoelectrics. The following table summarizes the different levels of efficiency calculation between these two mechanisms.

Mechanism		Thermoelectrics	VO <sub>2</sub> for actuation (this work)
Physical limit	Condition	$\kappa = 0, \sigma = \infty, ZT = \infty$	$c = 0, H = \infty$
	Efficiency	$\eta = \eta_{\text{Carnot}}$	$\eta = \eta_{\text{Carnot}}$
Materials limit (Only intrinsic loss included)	Condition	$\kappa > 0, \sigma < \infty, ZT$ finite. Intrinsic loss: heat conduction, Joule heat.	$c > 0, H < \infty$ . Intrinsic loss: heat capacity.
	Efficiency	$\eta < \eta_{\text{Carnot}}$ ; $\eta = 3.4\%$ for $ZT = 2.1$	$\eta < \eta_{\text{Carnot}}$ ; $\eta = 3.4\%$ for $c$ and $H$ of VO <sub>2</sub>
device limit (Extrinsic loss also included)	Condition	Additional extrinsic loss: air heat loss, contact resistance loss, etc.	Additional extrinsic loss: air heat loss, friction loss, etc.
	Efficiency	$\eta < 3.4\%$ for $ZT = 2.1$	$\eta < 3.4\%$ for $c$ and $H$ of VO <sub>2</sub>

## 8. Calculation of cantilever resonant frequency

From beam theory, we know the spring constant for a simple beam in transverse oscillation<sup>xi</sup> is given by

$$k = \frac{F}{\delta} = \frac{3EI}{L^3} \quad (\text{S12})$$

forming the general case of equation (S7), where the bending modulus (stiffness)  $EI$  is replaced by the expression for a bimorph. We find the resonant frequency  $f_n$  with the relation

$$f_n = \frac{1}{2\pi} \sqrt{\frac{k}{m_{\text{eff}}}} \quad (\text{S13})$$

where  $m_{\text{eff}} = \frac{33}{140}m = \frac{33}{140}\rho abL$  is used, since the beam mass is distributed (resulting in varying velocities) along the oscillation length. For a beam sharing the dimensions in our experiment and the frequency calculations of thermal transport in the main text ( $L = 150 \mu\text{m}$ ,  $a = 700\text{nm}$ ,  $b_1 = 700\text{nm}$ ,  $b_2 = 200\text{nm}$ ), the resonant frequency is calculated to be 1.29 MHz, significantly higher than the frequencies examined by pulsed optical excitation. Thus the rise in deflection amplitudes at intermediate frequencies is not attributed to resonance, but rather the M2-R transition.

- 
- <sup>i</sup> Rua, A.; Cabrera, R.; Coy, H.; Merced, E.; Sepulveda, N.; Fernandez, F. E. Phase Transition Behavior in Microcantilevers Coated with M<sub>1</sub>-phase VO<sub>2</sub> and M<sub>2</sub>-phase VO<sub>2</sub>:Cr Thin Films. *J. Appl. Phys.* **2012**, *111*, 104502.
- <sup>ii</sup> Cao, J.; Gu, Y.; Fan, W.; Chen, L. Q.; Ogletree, D. F.; Chen, K.; Tamura, N.; Kunz, M.; Barrett, C.; Seidel, J. *et al.* Extended Mapping and Exploration of the Vanadium Dioxide Stress-Temperature Phase Diagram. *Nano Lett.* **2010**, *10*, 2667–2673.
- <sup>iii</sup> Shen, D.; Park, J.-H.; Ajitsaria, J.; Choe, S.-Y.; Wickle, H. C.; Kim, D.-J. The Design, Fabrication and Evaluation of a MEMS PZT Cantilever with an Integrated Si Proof Mass for Vibration Energy Harvesting. *J. Micromech. Microeng.* **2008**, *18*, 055017.
- <sup>iv</sup> Cao, J.; Fan, W.; Zhou, Q.; Sheu, E.; Liu, A.; Barrett, C.; Wu, J. Colossal Thermal-mechanical Actuation via Phase Transition in Single-crystal VO<sub>2</sub> Microcantilevers. *J. Appl. Phys.* **2010**, *108*, 083538.
- <sup>v</sup> Timoshenko, S. Analysis of Bi-Metal Thermostats. *J. Opt. Soc. Am.* **1925**, *11*, 233–255.
- <sup>vi</sup> Berglund, C. N.; Guggenheim, H. J. Electronic Properties of VO<sub>2</sub> Near the Semiconductor-Metal Transition. *Phys. Rev.* **1969**, *185*, 1022–1033.
- <sup>vii</sup> Williams, I. S.; Gopal, E. S. R.; Street, R. The Specific Heat of Strained and Annealed Chromium. *Journal of Physics F: Metal Physics* **1979**, *9*, 431–445.
- <sup>viii</sup> Cao, J.; Ertekin, E.; Srinivasan, V.; Fan, W.; Huang, S.; Zheng, H.; Yim, J. W. L.; Khanal, D. R.; Ogletree, D. F.; Grossman, J. C. *et al.* Strain Engineering and One-dimensional Organization of Metal-insulator Domains in Single-crystal Vanadium Dioxide Beams. *Nature Nanotech.* **2009**, *4*, 732–737.
- <sup>ix</sup> McWhan, D. B.; Marezio, M.; Remeika, J. P.; Dernier, P. D. X-ray Diffraction Study of Metallic VO<sub>2</sub>. *Phys. Rev. B* **1974**, *10*, 490–495.
- <sup>x</sup> Straumanis, M. E.; Weng, C. C. The Precise Lattice Constant and the Expansion Coefficient of Chromium Between +10 and +60° C. *Acta Crystallographica* **1955**, *8*, 367–371.
- <sup>xi</sup> Stokey, W. F. Vibration of Systems Having Distributed Mass and Elasticity. In *Shock and Vibration Handbook*; Harris, C.M., Crede, C.E., Eds.; McGraw-Hill: New York, 1976), pp 7.1 – 7.18